

Cementitious composites reinforced with 3D printed functionally graded polymeric lattice structures

Experiments and modelling

Xu, Yading; Zhang, Hongzhi; Gan, Yidong; Šavija, Branko

DOI

[10.1016/j.addma.2021.101887](https://doi.org/10.1016/j.addma.2021.101887)

Publication date

2021

Document Version

Final published version

Published in

Additive Manufacturing

Citation (APA)

Xu, Y., Zhang, H., Gan, Y., & Šavija, B. (2021). Cementitious composites reinforced with 3D printed functionally graded polymeric lattice structures: Experiments and modelling. *Additive Manufacturing*, 39, 1-13. Article 101887. <https://doi.org/10.1016/j.addma.2021.101887>

Important note

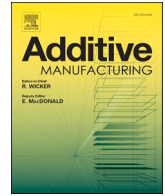
To cite this publication, please use the final published version (if applicable). Please check the document version above.

Copyright

Other than for strictly personal use, it is not permitted to download, forward or distribute the text or part of it, without the consent of the author(s) and/or copyright holder(s), unless the work is under an open content license such as Creative Commons.

Takedown policy

Please contact us and provide details if you believe this document breaches copyrights. We will remove access to the work immediately and investigate your claim.



Research Paper

Cementitious composites reinforced with 3D printed functionally graded polymeric lattice structures: Experiments and modelling

Yading Xu, Hongzhi Zhang^{*}, Yidong Gan, Branko Šavija

Microlab, Delft University of Technology, The Netherlands

ARTICLE INFO

Keywords:

Cementitious composites
Polymeric reinforcement
Functionally grade
3D printing

ABSTRACT

Cementitious materials are widely used in construction. For their low ductility, they typically need to be reinforced by steel rebars, which cause potential corrosion problems. Polymeric reinforcement, which does not have corrosion problems, has been used to replace steel rebars. However, a relatively high reinforcing ratio is usually required for the cementitious composites reinforced by conventional polymeric reinforcement. Owing to the customizability of 3D printing technology, polymeric reinforcement with a functionally graded structure is able to be manufactured, which significantly reduces the reinforcing ratio of the reinforced cementitious composites meanwhile improves their mechanical properties. In this present study, 3D printed polymeric octet lattice structures were used as reinforcement to develop cementitious composites with enhanced ductility. Four-point bending experiments were performed on the plain mortar, and the reinforced specimens and a finite element model was used to simulate the experiments numerically. A good agreement between experiments and simulations was found: the reinforced specimens have a significantly increased flexural ductility comparing to plain mortar. Composites reinforced by vertically functionally graded lattice structures have a significantly lower reinforcing ratio while exhibiting obviously higher normalized ductility. In addition, the fracture behavior of the reinforced cementitious composites was evaluated using a fracture energy based analytical model. The analysis shows that, from the perspective of fracture energy release, the steady state cracking criteria were not satisfied by the cementitious composites developed in this study so that multiple cracking and strain hardening behavior was not obtained. However, according to numerical predictions, increasing strength of the printed reinforcement material by 40% would allow these behaviors to be potentially achieved. This work shows that additive manufacturing has great potential for developing reinforcement for cementitious materials to reduce the reinforcing ratio and enhance ductility.

1. Introduction

In recent years, digitalized construction has been more and more popular in the field of civil engineering. Among these digitalized construction processes, additive manufacturing, commonly called 3D printing, has attracted attention for its possibilities in the manufacturing of cementitious materials [1–4]. As the most widely used construction materials, the main drawback of cementitious materials is their lack of ductility, namely, they have low tensile strength and prone to cracking [5,6]. Traditionally, steel rebars are used as reinforcement to improve the ductility of cementitious materials. Depending on the loading conditions, steel rebars need to be manually placed at the positions with high tensile or shear stress such that no catastrophic failure occurs after the cementitious matrix cracking. However, reinforcement corrosion is a

critical issue when cementitious materials are reinforced by steel rebars. Corrosion of the steel rebars causes expansion inside the cementitious matrix and potential internal cracking appears as a result [7,8]. The cracked matrix may cause further corrosion as the aggressive ingredients penetrate easier through the cracks [9–11]. Fibers have been used as reinforcement materials to replace steel rebars [12–15]. A typical type of fiber reinforced cementitious material are engineering cementitious composites (ECC) [12], also known as the strain hardening cementitious composites (SHCCs) [16,17] in which PVA (Polyvinyl alcohol) fibers are often used as the reinforcement material. The main feature of this type of fiber reinforced cementitious composites is the so-called multiple cracking and pseudo strain hardening behavior in uniaxial tension: the SHCCs are able to crack multiple times before eventual failure, while the ultimate failure strength is higher than their first cracking strength.

^{*} Corresponding author.

E-mail addresses: Y.Xu-5@tudelft.nl (Y. Xu), hzzhang@sdu.end.cn (H. Zhang), y.gan@tudelft.nl (Y. Gan), b.savija@tudelft.nl (B. Šavija).

<https://doi.org/10.1016/j.addma.2021.101887>

Received 3 August 2020; Received in revised form 16 January 2021; Accepted 1 February 2021

Available online 10 February 2021

2214-8604/© 2021 The Author(s). Published by Elsevier B.V. This is an open access article under the CC BY license (<http://creativecommons.org/licenses/by/4.0/>).

Owing to this, the SHCCs have significantly higher ductility compared to plain cementitious materials. The fiber reinforced cementitious materials also have their limitations. Normally, only very limited types of fibers are able to be used to develop the SHCCs as the requirement for surface modification [18] of the fibers is rather strict in order to achieve proper crack bridging. Worldwide, only a few manufacturers are able to produce such fibers and the price is rather high. In addition, fiber orientation is another issue: fibers that are not perpendicular to the crack surface have reduced crack bridging ability, which decreases the efficiency of the fiber reinforcement.

Recently, more and more studies are focusing on using 3D printing technology to produce reinforced cementitious materials. One approach is to directly print reinforced cementitious material, such as fiber reinforced cementitious composites [19–21] or cable reinforced cementitious materials [22,23]. During the extruding process, fibers or a cable are able to be aligned to the printing direction due to the extrusion so that reinforcement can be orientated to increase crack bridging ability parallel to the printing direction. However, this also introduces anisotropy in the cementitious material. Another approach is to print the reinforcement first and then cast cementitious material afterwards, such as using 3D printed steel bars [24], steel bolts [25] or metallic fibers [26, 27] as reinforcement. In these cases, owing to the customizability of 3D printing, the surface roughness can be tailored [24,27] to enhance the bond between the reinforcement and the cementitious matrix such that the performance of the reinforced cementitious can be improved. Comparing to printing metal and metallic material, 3D printing polymeric materials are much more accessible and economical in terms of the requirement for printing equipment, production of raw material, and printing cost. Numerous types of polymeric filaments [28–30] or ink [31,32] are easily accessible and can be used even on desktop 3D printers to manufacture polymeric objects with good printing quality. Previously, 3D printed polymeric structures have been proved capable of creating the SHCCs [33,34] when used as reinforcement while a relatively high reinforcing ratio was required. For three-dimensional lattice structures, functionally grading is an efficient method to improve properties at minimal material use [35,36], which could possibly be used to reduce the reinforcing ratio of the cementitious composites. Depending on the loading conditions, structural parameters such as lattice cell density and lattice cell size can be functionally graded such that the lattice structures exhibit equivalent or even better properties, for example, specific stiffness and energy absorption [35–38].

In this work, three-dimensional polymeric octet lattice structures are 3D printed and used as reinforcement for cementitious mortar. The octet lattice structures are functionally graded to optimize the flexural ductility of the cementitious composites, meanwhile minimizing the reinforcing ratio. Flexural behavior of the reinforced cementitious composites was experimentally and numerically studied and critically discussed. Adopting the experimental and numerical results, crack bridging ability of the reinforced cementitious composites is further analytically investigated. Based on these analyses, suggestions for future potential methods to enhance the performance of the cementitious composites are given.

2. Experiment methods

2.1. 3D printing of lattice reinforcement

Four different lattice structures were designed, printed, and used as reinforcement. An octet structure (see Fig. 1) was used as a unit cell of the lattice structures. The reinforcement lattice structures were designed by combining the unit cells of different sizes. Both in the longitudinal and the vertical direction, the reinforcement lattice structures were functionally graded according to the bending moment and tensile stress distribution (see Fig. 2), respectively. In the longitudinal direction, a smaller cell length was used in the middle so that more material locates in the maximum moment region at mid span. In the vertical direction,

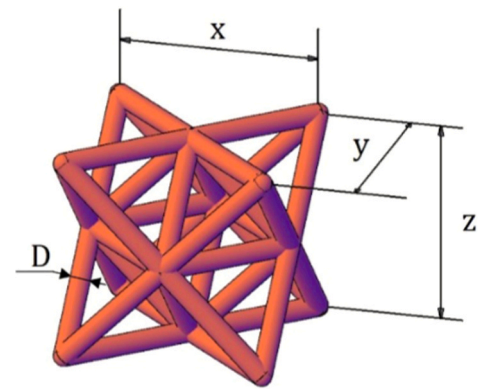


Fig. 1. Unit cell of the lattice structure, x, y and z are the dimensions of a unit cell in three directions, D is the diameter of the lattice strut, detail information of used unit cells can be found in Table 1.

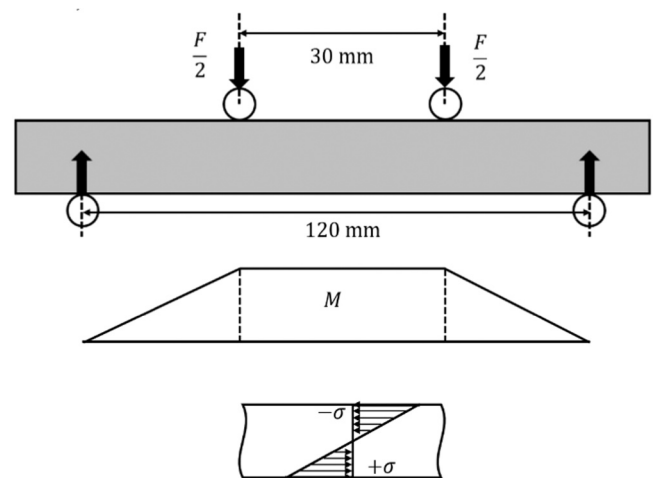


Fig. 2. Schematics of four-point bending, distribution of bending moment and stress on the loaded specimen is shown, maximum bending moment exists at the mid span of the specimen and highest tensile stress exists at the bottom of the specimen mid span.

because tensile stress is linearly distributed on the specimen cross section (see Fig. 2), the diameter of the lattice struts was also functionally graded, ensuring that more material was used at the bottom which had higher tensile stress. This was done by linearly increasing the strut diameter from 3 mm to 2 mm bottom up. Dimensional parameters of all used unit cells are listed in Table 1. The configuration of these unit cells in four designed lattice structures are shown in Fig. 3. Note that four “studs” were also designed for each reinforcement structure, ensuring they can be easily positioned in the molds during casting. All designed lattice structures are printed accordingly and then used as reinforcement for cementitious mortar under four-point bending tests, description of experimental test groups is listed in Table 2.

Table 1
Dimensional parameters of the used unit cells.

Unit Cell	x (mm)	y (mm)	z (mm)	D (mm)
C10	10	20	20	3
C15	15	20	20	3
C25	25	20	20	3
C40	40	20	20	3
RC10	10	20	20	2 (top) ~ 3 (bottom)
RC15	15	20	20	2 (top) ~ 3 (bottom)
RC25	25	20	20	2 (top) ~ 3 (bottom)
RC40	40	20	20	2 (top) ~ 3 (bottom)

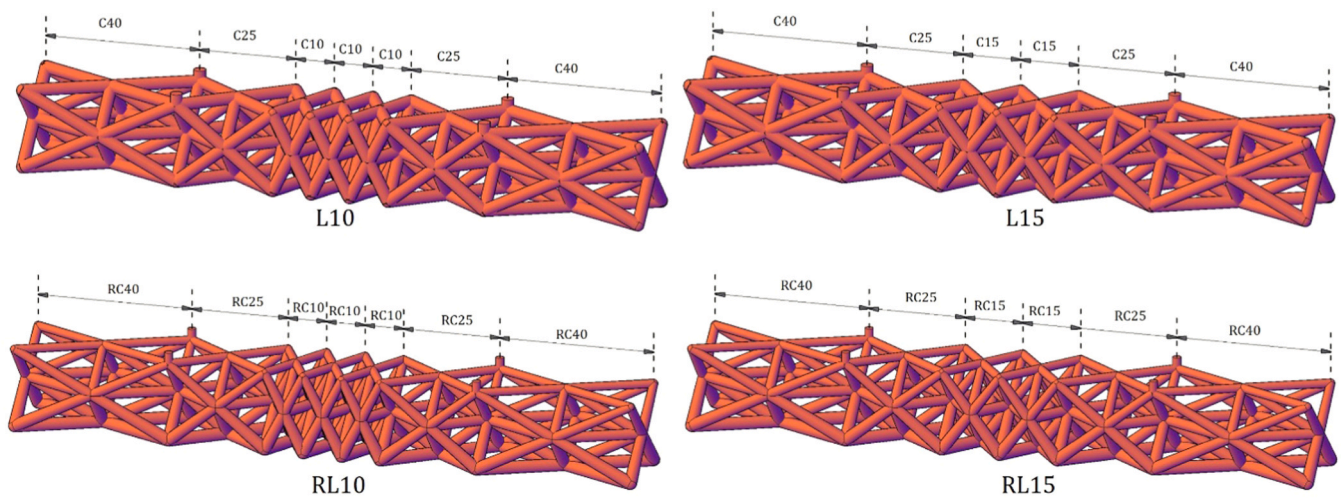


Fig. 3. Designed functionally graded octet lattice structures, unit cells are indicated, “C” and “RC” indicate the type of used unit cells, dimensions of these unit cells can be found in Table 1.

Table 2
Testing groups.

No.	Volumetric reinforcing ratio	Description
REF	0%	Reference
L10	10.13%	Unit cell size graded in longitudinal direction with C10 cell in the middle
L15	11.22%	Unit cell size graded in longitudinal with C15 cell in the middle
RL10	5.78%	L10 with strut diameter functionally grade in height direction
RL15	5.32%	L15 with strut diameter function grade in height direction

The designed reinforcement lattice structures were printed using a fuse deposition modeling (FDM) commercial 3D printer Ultimaker 2+. Considering the alkaline environment of cementitious materials, ABS (Acrylonitrile Butadiene Styrene), which has high chemical resistance, was used as the printing filament material. Printing parameters for all four designs were kept constant and listed in Table 3. As the reinforced specimens were designed to be flexural loaded, the maximum tensile stress will be present at the bottom of the specimen as well as the reinforcement lattice structure. In order to ensure the reinforcement with maximum tensile resistance [39], the printing direction of the lattice structures was arranged such that the printed layers are parallel to the tensile stress direction (shown in Fig. 4c). The printed lattice structures were placed inside the Styrofoam molds, and the “studs” were glued on the molds by silicone rubber making sure the reinforcement unable to detach from the molds during vibration (see Fig. 4c). The casted specimens had dimensions of 40 mm × 40 mm × 160 mm. In addition, in order to obtain input parameters for numerical simulations, dog bone shaped ABS bars with a cross section of 3 mm × 3 mm were printed and tested in uniaxial tension (shown in Fig. 4b).

Table 3
Printing parameters.

Printing parameter	Configuration
Nozzle diameter (mm)	0.8
Temperature (°C)	260
Layer height (mm)	0.25
Line width (mm)	0.7
Infill density (%)	100

2.2. Casting and curing

In order to properly compare mechanical properties of the mortar bars reinforced with 2D structures reported in [33], the same matrix and reinforcement materials, reinforcement printing parameters and specimens preparing procedures are used. The mix proportion of the mortar used is listed in Table 4.

Dry materials (cement, fly ash, and sand) were first weighted and mixed using a Horbart machine for four minutes. Superplasticizer and water were weighted together and added to the dry mix. All materials were mixed for additional four minutes. Then the mixed materials were cast inside Styrofoam molds and vibrated for 30 s. Afterwards, the specimens were cured in room temperature for one day, and plastic films were covered on top of the casted specimens to prevent water evaporation. After one day, the specimens were demolded and cured in a curing chamber (96% ± 2%RH, 20 ± 2 °C) for 27 days until the age of 28 days. One hour before test, the specimens were taken out of the curing chamber and painted on one surface by white background and black dots for DIC analysis used for measuring crack mouth opening displacement (CMOD). In order to obtain compressive and tensile parameters needed for the numerical model, cementitious mortar cubes (15 mm × 15 mm × 15 mm) and cementitious mortar bars (30 mm × 10 mm × 100 mm) were also cast and cured at the same condition until the same age. These specimens were then tested under uniaxial compression and tension, respectively.

2.3. Mechanical tests

Four-point bending tests were performed on all the prepared specimens by a servo hydraulic press (INSTRON 8872). Loading was applied on the top of the specimens under displacement control with a constant rate 0.01 mm/s. The loading scheme and the experimental setup of the four-point bending test are shown in Fig. 5. Note that the reinforcement structure shown in Fig. 3 was optimized for this specific loading setup: if a different loading setup were used, the middle region (i.e., the region with the maximum bending moment in Fig. 5a where a denser lattice mesh was printed) would have been different. A digital camera was placed in front of the specimen to take pictures for DIC. During the test load and deflection (vertical displacement at the middle of the specimens) was measured by Instron 8872. After the first main crack appeared, crack mouth opening displacement (CMOD) was measured by DIC. Uniaxial compression and tension tests were performed on cementitious mortar cubes, mortar bars and ABS bars respectively to obtain compressive and tensile stress-strain curves for calibration the

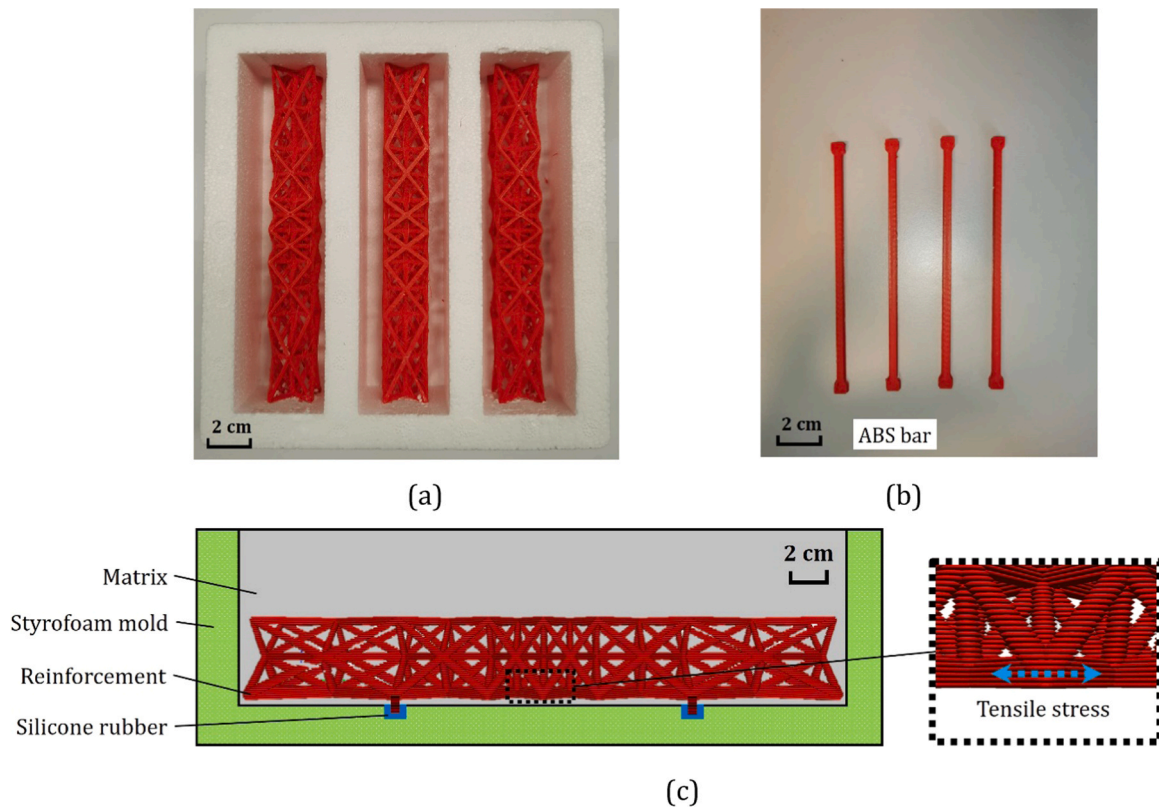


Fig. 4. Schematics of a) printed specimens and Styrofoam mold; b) the printed ABS bars; c) positioning of specimen in Styrofoam mold during casting.

Table 4
Mix proportion of the matrix material(kg/m³), adopted from [33].

CEM I 42.5 N	Fly ash	Sand (0.125–0.250 mm)	Superplasticizer (Glenium 51)	Water
550	650	550	2	395

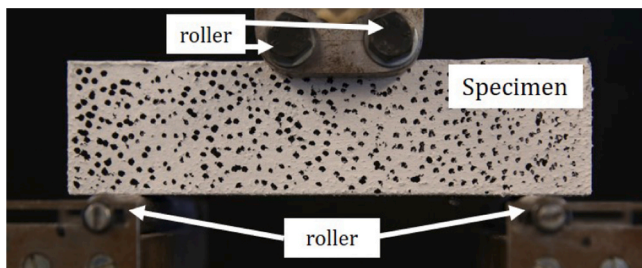


Fig. 5. Four-point bending experimental setup.

numerical models.

3. Numerical simulations

3.1. Concrete damaged plasticity model (CDPM)

A commercial FEA software ABAQUS/Explicit was used to simulate the four-point bending tests. In terms of simulating damage process of cementitious materials, concrete damaged plasticity model (CDPM) are commonly used as the material model for cementitious matrix.

The constitutive equation of CDPM is written as follows:

$$\sigma = (1 - d)E_0(\varepsilon - \varepsilon^{pl}) \quad (1)$$

Where is σ Cauchy stress; ε and ε^{pl} are total strain and equivalent plastic strain, respectively; E_0 is initial elastic modulus. d is damage variable and can be defined from 0 to 1. In this study, as the matrix is brittle stiffness degradation is not considered, then $d = 0$.

The damage in CDPM is characterized by compressive plastic strain $\tilde{\varepsilon}_c^{pl}$ and tensile plastic strain $\tilde{\varepsilon}_t^{pl}$, respectively. As shown in Fig. 6, the stress σ_{c0} and σ_{tu} indicate the onset of in-elastic stage under compression and tension. The compressive inelastic strain (ε^{in}) and tensile cracking strain (ε^{ck}) is defined as the total strain minus the elastic strain, respectively. As mentioned previously, in this study the damage parameter d in Eq. (1). is taken as 0, then compressive plastic strain $\tilde{\varepsilon}_c^{pl} = \varepsilon^{in}$ and tensile plastic strain $\tilde{\varepsilon}_t^{pl} = \varepsilon^{in}$.

3.2. Model calibration and validation

Prior to simulating the four-point bending tests, calibration and validation procedures were performed to obtain proper material compressive and tensile input parameters. Considering the accuracy and computational cost, 2 mm hexahedron elements were used for the cementitious matrix and 2 mm tetrahedron elements were used for ABS reinforcement. The mesh size was kept constant for all numerical simulations in this study. In order to model the interaction between the cementitious matrix and reinforcement, the “embedded region” constraint was assigned for the reinforcement composites using the cementitious matrix as host region and the printed reinforcement structure as embedded region. Table 5 shows the physical properties of cementitious mortar and input parameters for CDPM. Elastic modulus, density and Poisson’s ratio were measured from experiments, other parameters were adopted using ABAQUS default values. By trial and error, the compressive and tensile input parameters were calibrated through varying the input parameters so that the simulated compressive and tensile stress-strain curves fit the experimental results. In order to simulate the damage process of cementitious matrix and ABS

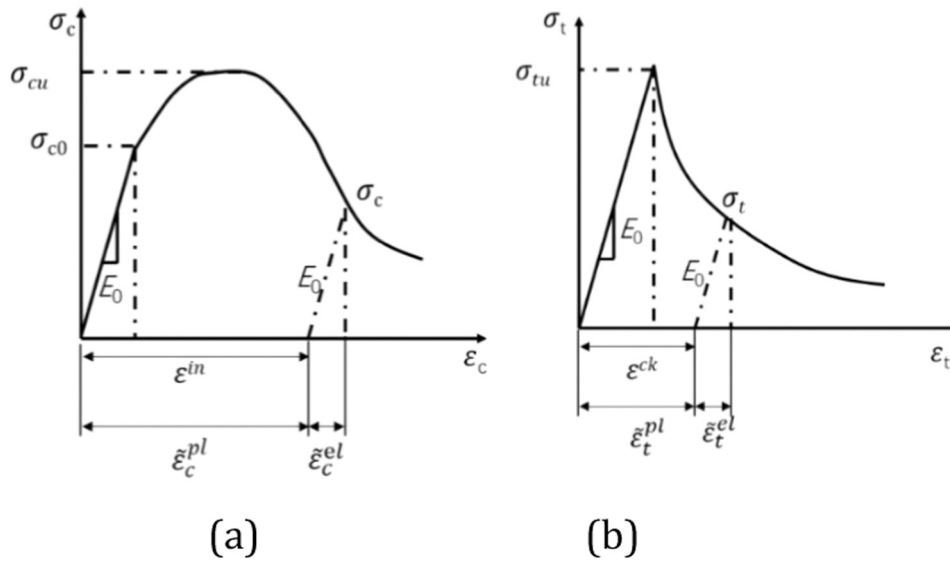


Fig. 6. Constitutive law of CDPM in a) compression and b) tension.

Table 5
Input parameters for CDPM.

Material input parameters	Value
Density (kg/m ³)	1870
Elastic Modulus (MPa)	15,500
Poisson's Ratio	0.2
Dilation Angle (°)	35
Eccentricity	0.1
fb0/fc0	1.16
K	0.667
Viscosity Parameter	0.001

Table 7
Tensile parameters of cementitious mortar.

Yield Stress (MPa)	Cracking strain
5.8	0
0.1	0.0005

Table 8
Tensile parameters of ABS reinforcement.

Direct stress after cracking (MPa)	Direct cracking strain
25	0
20	0.2
0.1	0.25

reinforcement, respectively, the CDPM material model was used for cementitious mortar while brittle cracking material model was used for ABS reinforcement. Numerical uniaxial compression tests were performed on the cubic mortar specimens to calibrate the cementitious matrix compressive parameters. Input parameters of cementitious mortar and ABS reinforcement are listed in Tables 6–8. The comparison of calibrated compression curve and experimental curves are shown in Fig. 7a. Similarly, numerical uniaxial tension tests were performed on the mortar and ABS bars to validate tensile input parameters of the cementitious matrix and ABS reinforcement. The comparison of calibrated compression curve and experimental curves are shown in Fig. 7b and c.

3.3. Four-point bending simulation

Corresponding to experiment setup, numerical four-point bending tests were performed. In order to decrease the computational cost, symmetrical boundary conditions were used, and half of the actual specimen (shown in Fig. 8) was numerically simulated. Four rigid rollers were generated as loading and supporting devices on the top and bottom of the specimen. A minor friction coefficient (0.15) was assigned between the loading rollers and the specimen to prevent unrealistically

Table 6
Compressive parameters of cementitious mortar.

Yield stress (MPa)	Inelastic strain
38	0
42	0.00149
3	0.0018
1	0.002

large lateral movement of the specimen in the case of an ideal frictionless contact. Downwards displacement was applied on the two upper loading rollers, while all degrees of freedom of bottom loading rollers are completely fixed (Fig. 8). Plain mortar specimens and the four reinforced specimens are numerically tested. The results of numerical simulations are discussed in detail in the next section.

4. Results and discussion

4.1. Flexural stress-deflection response

The comparison of experiments and simulated stress-deflection curves of the four-point bending test are shown in Fig. 9. A good agreement can be found between experiment (red curves) and numerical simulation (black curve) results. For the plain specimen (see Fig. 9a REF), as no reinforcement was used brittle cracking behavior, witnessed by a sudden load drop as deflection increases, can be observed on the stress-deflection curves. The flexural strength of plain mortar reaches around 5.8 MPa at 28 days, which is somewhat higher than the flexural strength (5.0 MPa) reported in [33] for the same mix. This difference can be attributed to the fact that in [33] a much thinner specimen was used, which could be more sensitive to the influence of small defects such as air voids on flexural strength.

On the other hand, it can be seen from Fig. 9b to e that all reinforced specimens show ductile stress-deflection response (witnessed by a significant drop followed by a second peak with hardening and softening branch on the stress-deflection curve). This ductile stress-deflection

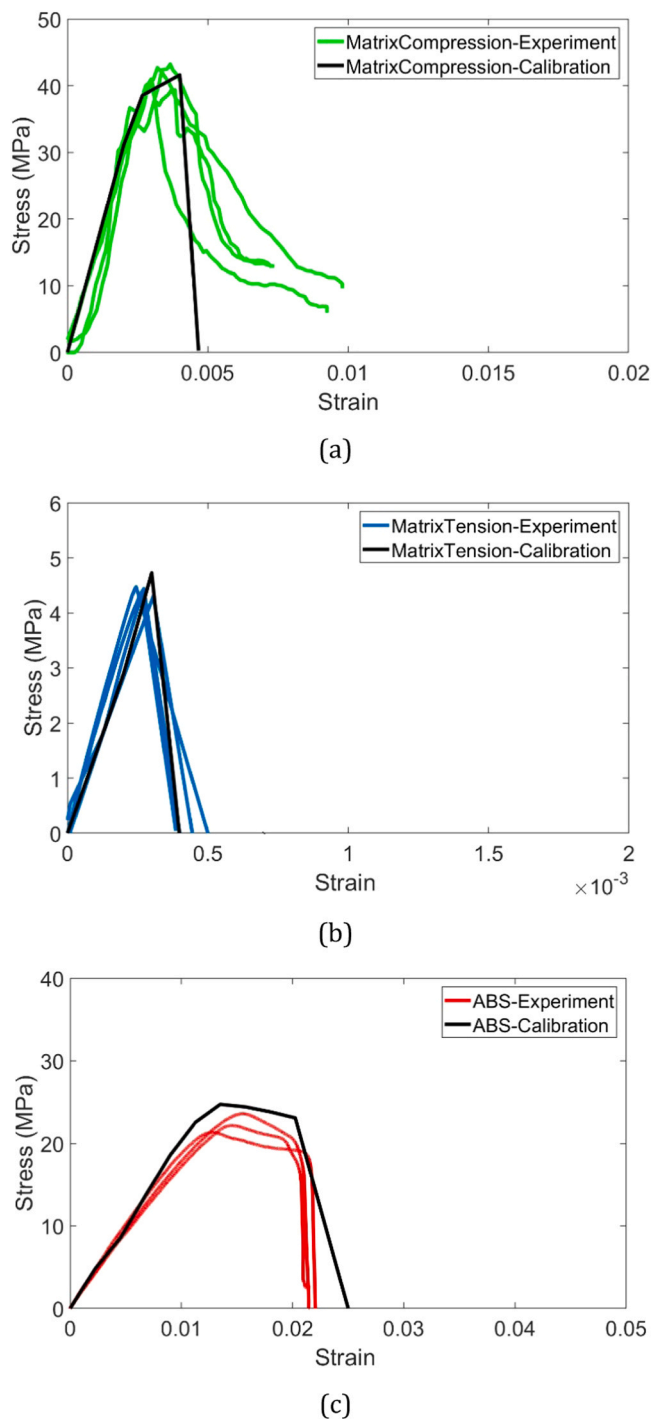


Fig. 7. Calibrated stress-strain curve of cementitious mortar in a) compression, b) tension and c) ABS reinforcement in tension.

response clearly indicates that the brittle cracking failure of cementitious mortar was significantly changed by the reinforcing octet lattice structures to ductile failure. The failure process of all reinforced specimens is shown in Fig. 11, as the symmetric boundary condition was used for simulation, the symmetrical mirrored results using the symmetrical boundary plane are also shown. As CDPM was used as a material model for the cementitious matrix, the model element damage is then indicated by plastic strain, and the cracks are the regions with non-zero plastic strain. The entire failure process of the reinforced cementitious mortar can be described by two stages. The first stage corresponds to the first peak on the stress-deflection curve which indicates the brittle cracking

of cementitious matrix (deflection ranges from $d = 0$ to $d = 0.06$ mm). Similar to plain mortar, when flexural load was applied, the highest tensile load generated at the bottom mid span of the reinforced specimen. As soon as the tensile stress reaches the tensile strength of the cementitious mortar (5.8 MPa), a crack initiates at the bottom of the specimen and rapidly propagates to the top side. As shown in Fig. 11, the main crack occurs at the mid span of each of the reinforced specimens when the deflection reaches 0.06 mm. It is shown in Fig. 10 that both in experimental and simulation results the plain mortar specimens (REF) have the highest flexural cracking strength (6.33 MPa from experiment and 6.17 MPa from simulation) while the reinforced specimens have relatively lower flexural cracking strength. This is because the reinforcement has a lower elastic modulus than the cementitious matrix, comparing to the plain mortar, the neutral axis of the reinforced composites is shifted closer to the top side of the specimen. As a result, under the same bending moment, higher tensile stress will occur at the bottom side of the reinforced composites. In addition, due to the fact that experimental specimens may contain defects such as entrapped air voids due to improper vibration, especially when complex reinforcement structures are used, the simulated flexural cracking strength is also relatively higher than the experiment of these reinforced specimens.

After the first main crack, the reinforcement takes over the tensile load. Consequently, the flexural stress in reinforced specimens increased again until a second peak was reached, and a hardening branch can be observed during the fracture process (see Fig. 9). As deflection increases, the flexural load reaches a second peak, followed by a softening branch. During this process the crack opening increases continuously, witnessed by larger plastic strain (see Fig. 11, $d = 1$ mm). Eventually the reinforcement broke, leading to the failure of the reinforced composites. The fracture behavior of the reinforced composites is discussed in detail in the next section.

As mentioned before, with the presence of the hardening branch failure mode of the reinforced specimens is no longer brittle, but changed to ductile failure. The ductility of the reinforced specimens can be qualitatively and quantitatively characterized by ductility parameters. In this study, as shown in Fig. 12 two parameters are used to evaluate the ductility of the tested specimens: ductile failure strength σ_d (defined as the maximum stress after hardening branch) and the total work required to rupture the specimens (defined as the area surrounded by the flexural stress-deflection curve before 0.8 mm of deflection). In order to study the influence of the functionally grading, these two parameters are also normalized to the same volume of reinforcement according to the reinforcing ratio listed in Table 2. The ductile failure strength of all reinforced specimens is normalized relative to the same reinforcement volume of L10. The total work is normalized to per cubic centimeter of used reinforcement material.

Because plain mortar (REF) shows brittle cracking failure without any ductility, REF specimens have the ductile failure strength equal to zero, according to previous definitions. Comparatively, as the reinforced specimens exhibit ductile failure behavior, it can be seen from Fig. 13 that they have distinctly higher ductile failure strength. In addition, because of the ductile failure behavior of the reinforced specimens, the total work needed to rupture is also considerably increased comparing to the REF specimens. As shown in Fig. 14, the total work of the reinforced specimens increased 1200% (L10), 1143% (L15), 743% (RL10) and 785% (RL15), compared to the REF.

Among the reinforced specimens, L10 and L15 have higher reinforcing ratio (10.1% and 11.2% by volume) compared to RL10 (5.78%) and RL15 (5.32%), they have relatively higher ductile deflection capacity, ductile failure strength as well as higher total work of rupture than RL10 and RL15. However, in terms of the same amount of reinforcement, the normalized value gives a fairer comparison between the reinforced specimens. Ideally, under pure flexural loading condition, the tensile stress is linearly distributed along the height of the specimen so that the tensile stress at the bottom side of the specimen has a higher impact on the mechanical behavior. In this sense, the lattice struts of the

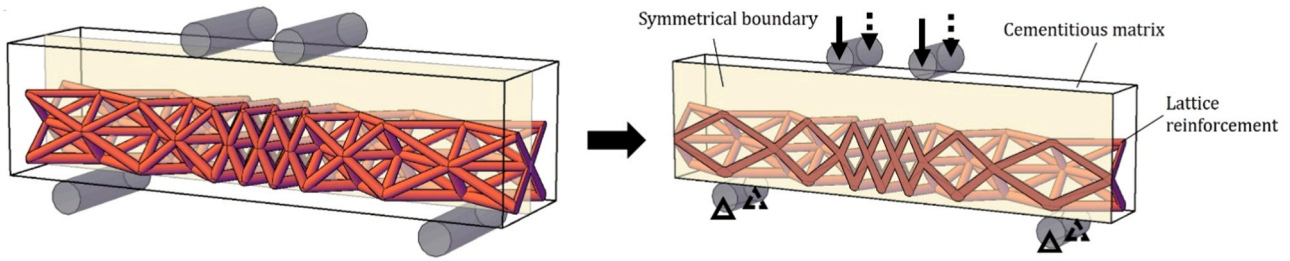


Fig. 8. Schematics of flexural loading condition in numerical simulation, half of the specimen was simulated under a symmetrical boundary condition.

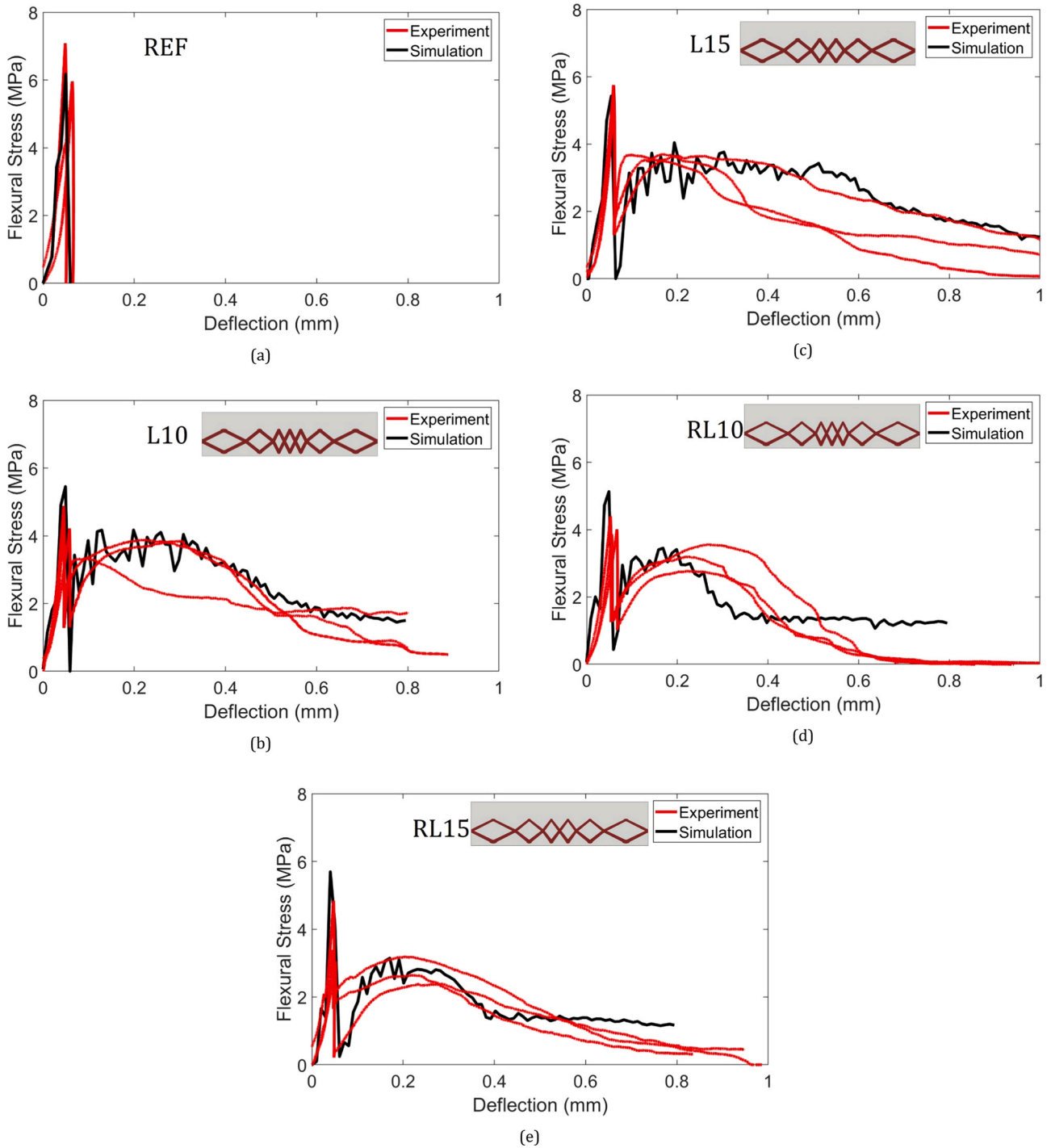


Fig. 9. Flexural stress-deflection curves of four-point bending tests, a) reference, b) L10, c)L15 d)RL10, e)RL15.

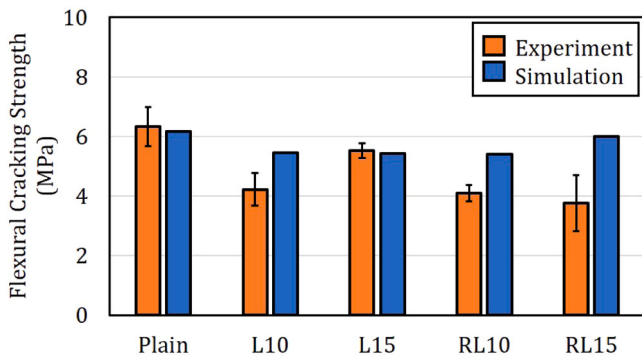


Fig. 10. Flexural cracking strength of all tested specimens obtained from experiments and simulations.

printed reinforcement at the bottom side always bear higher tensile stress in the ductile failure regime. Correspondingly, the radius of the lattice struts in RL10 and RL15 were functionally graded such that the reinforcement volume also linearly distributed along the height. It is clearly shown in Fig. 14 that both from experimental and simulated results, RL10 and RL15 contrarily have considerably higher ductile failure strength and total work comparing to L10 and L15 when the values are normalized to the same amount of reinforcement. Comparing to L10, RL10 increased 50.59% (52.40% from simulation) of the ductile failure strength and 13.34% (34.56% from simulation) of the total work meanwhile decreased 48.48% of reinforcement use. Comparing to L15, RL15 increased 57.18% (62.02% from simulation) of the ductile failure strength and 50.03% (42.30% from simulation) of the total work meanwhile decreased 47.48% of reinforcement use. A summary of ductile failure strength and total work of all tested specimens is given in Table 9.

According to previous analyses and discussions, from the qualitative point of view, the reinforced composites have shown ductile failure behavior. Quantitatively, the results of ductile failure parameter values also indicate a distinct increase in ductility of reinforced cementitious composites. More importantly, the ductile failure parameters also show that the functionally grading is very efficient in enhancing the flexural ductility of the cementitious materials while reducing the reinforcement use. In order to profoundly understand the failure mechanism as well as provide guidance in tailoring mechanical properties of the lattice structure reinforced cementitious composites, an in-depth analysis on the fracture behavior is provided in the next section.

4.2. Fracture behavior

Taking RL15 as an example, fracture behavior of the cementitious composites reinforced by functionally graded structure is discussed in detail in this section. Typically, notched specimens are preferred when studying the fracture behavior, however, in our study the bottom cementitious cover layer was rather thin and the cover layer thickness varied in different specimens. In this case, it was not possible to make a notch of the same size in all specimens. So, in our study making a notch is not the best choice. Instead, considering to the ductile failure behavior of the reinforced specimens, it was still possible to study the fracture behavior after the first main crack appeared in the cementitious matrix as long as crack opening can be measured. By digital image correlation (DIC), crack mouth opening displacement (CMOD) was obtained during the tests and the fracture behavior of the reinforced specimens are analyzed based on these data.

The experimental obtained and flexural load-CMOD curves of RL15 are shown in Fig. 15. Both from experiments and simulations, obvious hardening can be observed as the crack opening increases. Under four-point bending, a pure bending zone forms in the middle of the specimen. As a result, Mode I fracture condition was obtained and the

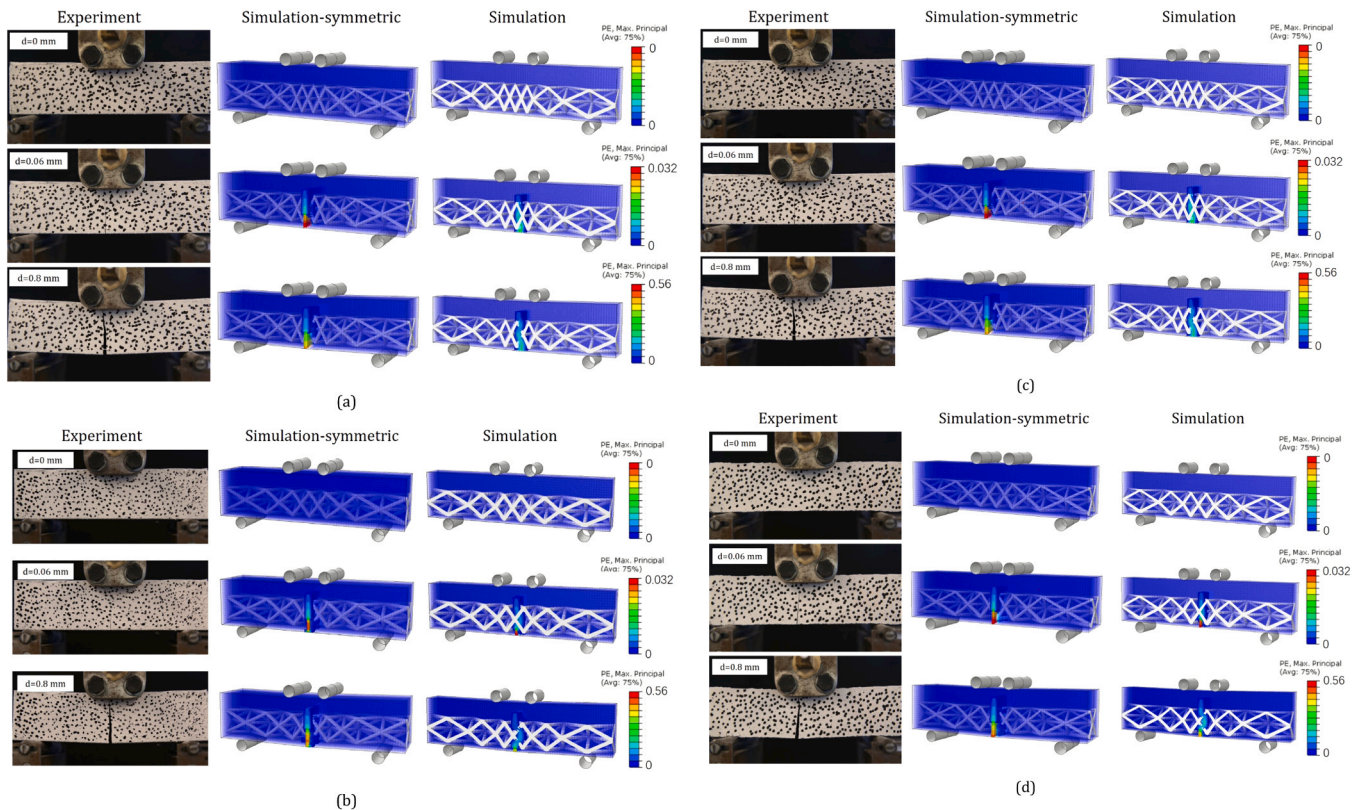


Fig. 11. Failure process of reinforced specimens obtained from experiments and simulations at different deflection, cracks are indicated by elements with non-zero plastic strain in the simulation; a) L10, b) L15, c) RL10, d) RL15; note that symmetrically mirrored simulation results are also shown.

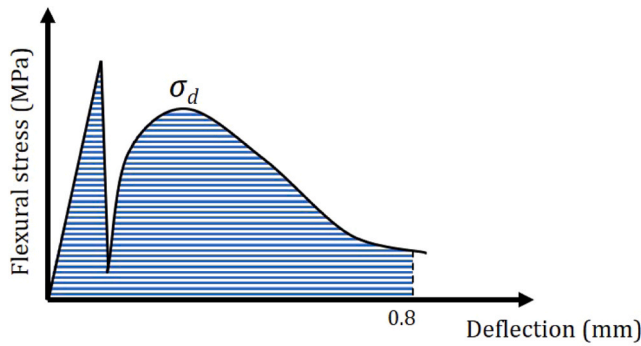


Fig. 12. A typical stress-deflection curve of reinforced cementitious composites, ductile failure stress (σ_d) and the total work of rupture (hatched area) is indicated.

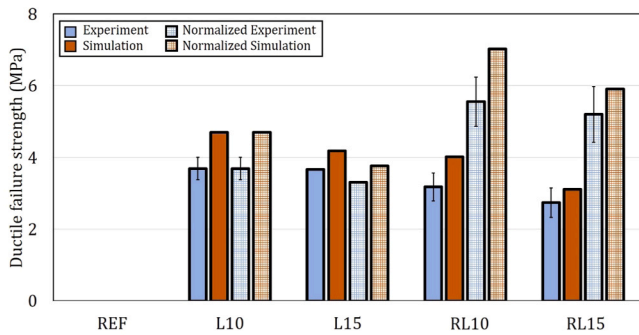


Fig. 13. Ductile failure strength and its normalized value, standard deviation is indicated for experiment results.

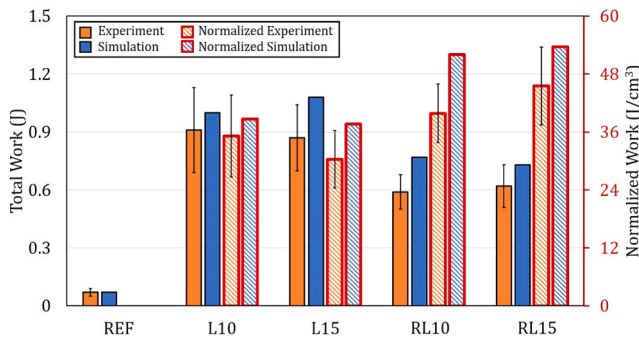


Fig. 14. Total work (left y axis) and normalized total work (right y axis) of all tested specimens, standard deviation is indicated for experiment results.

fracture process of the reinforced specimen is similar to that of fiber reinforced cementitious material with pseudo strain hardening behavior; namely, the crack is bridged by reinforcement phase between the generated crack surfaces. Because the struts constituting the lattices structure are connected within the cementitious matrix, pulling out of a single strut was not possible until the it was stretched to be completely broken. In addition, because the strength of the reinforcement is significantly higher than the matrix tensile strength, the crack bridging stress was only considered to be provided by the elastic stretching of lattice struts exposed across the generated crack surface until the strut broken (detaching and sliding between the reinforcement and the matrix interface might provide a minor crack bridging force, which was not considered in this study). The maximum crack bridging strength is then determined by the strength of the reinforcement material. As can be seen from the simulated black curve in Fig. 15, as CMOD increases the hardening branch reaches the flexural crack bridging strength at point

Table 9
Ductility parameters of the tested specimens.

No.	Ductile failure strength/ Simulation [MPa]	Normalized ductile failure strength/ Simulation [MPa]	Total work/ Simulation [J]	Normalized total work/ Simulation [J/cm ³]
Plain	0/0	0/0	0.07 (± 0.02)/ 0.07	0.07(± 0.02)/ 0.07
L10	3.69(± 0.31)/ 4.7	3.69(± 0.31)/ 4.7	0.91 (± 0.22)/ 1.00	35.19(± 8.51)/ 38.68
L15	3.67(± 0.02)/ 4.18	3.31(± 0.02)/ 4.18	0.87 (± 0.17)/ 1.08	30.34(± 5.93)/ 37.67
RL10	3.18(± 0.39)/ 4.02	5.56(± 0.68)/ 4.02	0.59 (± 0.09)/ 0.77	39.87(± 6.08)/ 52.04
RL15	2.74(± 0.41)/ 3.11	5.20(± 0.78)/ 3.11	0.62 (± 0.11)/ 0.73	45.52(± 8.07)/ 53.60

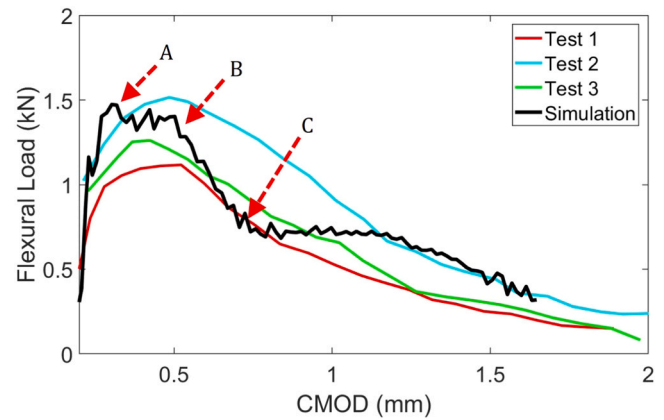


Fig. 15. Flexural load-CMOD curves of RL15, CMOD is measured by DIC.

“A”. Correspondingly, the tensile stress in the reinforcement increased up to its tensile strength (25 MPa, see Fig. 16). The point “A” indicates the onset of the reinforcement failure and the maximum fiber birding ability for a crack-open-hardening behavior. After point “A” the reinforcement started to fail, and as a result softening branch can be observed from the load-CMOD curves. It can be seen from Fig. 16 that from point “B” to point “C” the reinforcement generally cracked. Under ideal conditions, the tensile stress should be linearly distributed on the lattice strut from top to the bottom. However, due the heterogeneity of the cementitious matrix and the lattice structure, in reality after cracking a shear stress also exists inside the reinforcement struts so that the principle tensile stress distribution is not completely linear along the height direction.

Stress distribution inside the reinforcement struts exposed by the crack surface can also be analytically calculated adopting the transformed area method (see Fig. 17). As mentioned previously, it is assumed that elastic stretching of the exposed reinforcement struts provides the crack bridging force. Then, bending of the cracked cross section can be described by a transformed cross section combining the cross section of uncracked cementitious matrix A_m and the equivalent cross section A_i of the crack bridging reinforcement struts. A_i can be calculated by Eq. (2).

$$A_i = \frac{E_r}{E_m} S_i \quad (2)$$

Where S_i is the cross-sectional area of the reinforcement at a same height on the cross section; A_i is the equivalent cross-sectional area of the crack

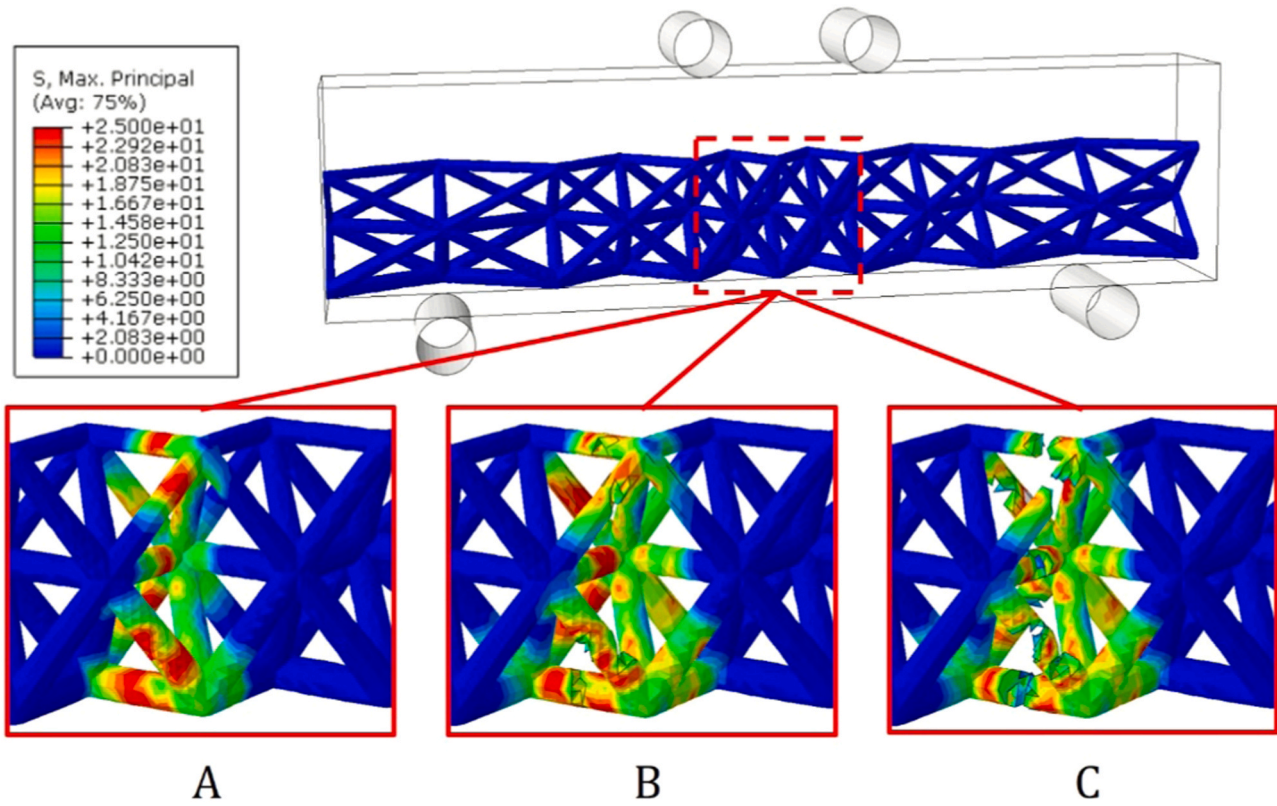


Fig. 16. Simulated failure process of the reinforcement corresponding to stress-CMOD curves.

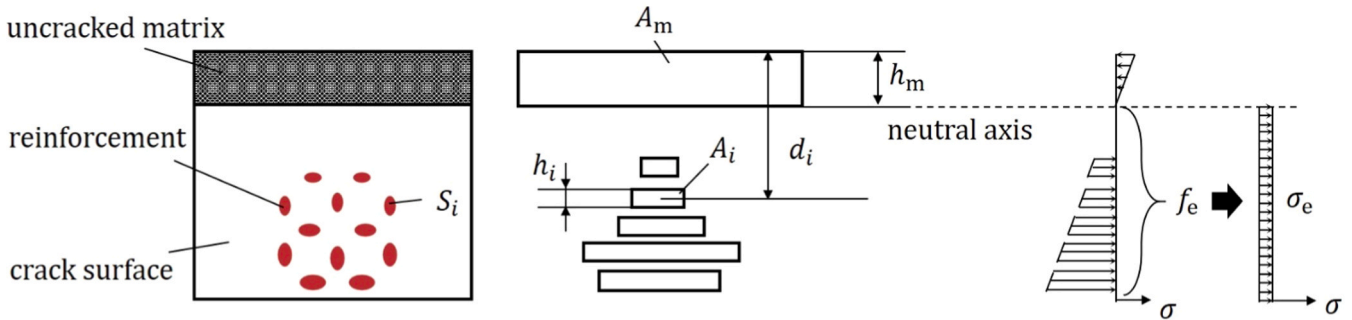


Fig. 17. Schematics of transformed cross section and the stress distribution.

bridging reinforcement at a same height; E_m and E_r are the elastic modulus of cementitious matrix and reinforcement, respectively.

The neutral axis coordinates y_i of the transformed cross section can be obtained by Eq. (3) and the moment of inertial of the equivalent cross section I_t can be obtained by Eq. (4).

$$y_i = \frac{A_m \frac{1}{2} h_m + \sum_1^i d_i A_i}{A_m + \sum_1^i A_i} \quad (3)$$

$$I_t = \frac{A_m h_m^2}{12} + A_m \left(\frac{h_m}{2} \right)^2 + \sum_1^i \left(\frac{A_i h_i^2}{12} + A_i (d_i - h_m)^2 \right) \quad (4)$$

Where are the y_m and y_i are the centroid coordinates of the uncracked matrix cross section and equivalent cross sections; A_m is the area of the uncracked matrix cross section; h_m is the height of the uncracked matrix section; h_i is the height of the equivalent cross sections, respectively. Using the neutral axis as the reference, then $y_i = 0$ and h_m can be

obtained.

After h_m is obtained, the moment of inertia I_t of the transformed cross section can be calculated by Eq. (4) and the equivalent strain of this transformed cross section ϵ can be calculated by Eq. (5).

$$\epsilon = \frac{My}{I_t E_m} \quad (5)$$

Then the stress within the reinforcement at the cracked cross section can be obtained using the data from flexural load-CMOD curve (Fig. 15). As the stress distribution varies along the height direction, the crack bridging stress of this cracked cross section needs to be calculated using the total force transferred within the reinforcement.

$$\sigma = \frac{\sum_1^i \sigma_i A_i}{A - A_m} \quad (6)$$

Where, A is the specimen cross section.

It is mentioned in the previous section that a hardening branch can

be observed on the load-CMOD curves. However, the peak load of this hardening branch is still lower than the cracking load of the cementitious matrix and the multiple cracking behavior typical of strain hardening cementitious composites (SHCC) was not observed in any of the tested specimens. This indicates that in the tested specimens, steady state cracking was not achieved and the generated cracks still followed Griffith type cracking behavior. Similar to SHCC, the energy release of cracking on the lattice reinforced cementitious composites can be determined by the J integral approach, as described in [40]. In order to obtain a steady state cracking, the crack bridging complementary energy J (Eq. 7) need to exceed the crack tip energy release rate J_{tip} . Under uniaxial tension condition:

$$J = \sigma_0 \delta_0 - \int_0^{\delta_0} \sigma \delta d\delta \quad (7)$$

As the crack tip is very small comparing to the specimen size in length and height, then under plain stress conditions it holds:

$$J_{tip} = K_I^2 / E_m \quad (8)$$

where, σ_0 is the crack bridging strength and δ_0 is the corresponding crack opening displacement. The crack bridging complementary energy is indicated by the hatched area (see Fig. 18). K_I and E_m are the fracture toughness and elastic modulus, respectively; K_I of plain cementitious mortar is normally $0.2\text{--}0.3 \text{ MPa}\sqrt{\text{m}}$.

However, under flexural loading conditions the flat crack surface cannot be achieved. Because the tensile stress on a cross section is distributed linearly along the height, for a given bending moment the crack opening varies along the height direction of the specimen. Then, an equivalent crack opening should be found. Because the stress is linearly distributed along the height of the crack cross section, it is reasonable to assume that the crack opening is also linearly distributed (see Fig. 19). In this sense, the equivalent crack opening of a cracked surface is half of the crack opening measured at the crack mouth then Eq. (7) is written as:

$$J_b = \frac{1}{2} \sigma_0 \delta_0 - \frac{1}{2} \int_0^{\delta_0} \sigma \delta d\delta \quad (9)$$

δ is the measured CMOD at the bottom of the cracked specimen; σ is the crack bridging stress which can be obtained by Eq. (6). using the experimental and numerical simulated flexural load-CMOD data. The calculated complementary energy J_b results are shown in Fig. 20.

Due to the heterogeneity of the cementitious composites, in order to achieve the so-called multiple cracking behavior, a quite large margin value is required for the complementary energy J_b . It has been proved by [41] that for some fiber reinforced composites, J_b needs to be at least

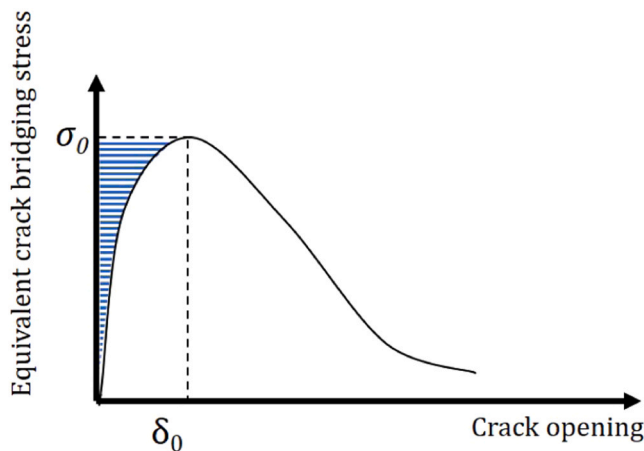


Fig. 18. Schematics of crack bridging stress-crack opening curve, the shaded area indicates the crack bridging complementary energy [12,40].

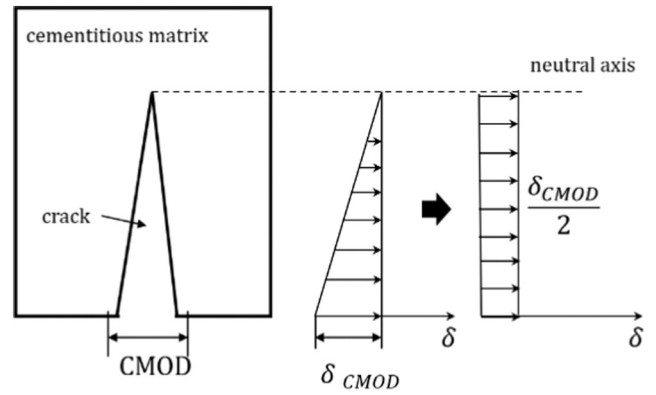


Fig. 19. Equivalent crack opening under flexural load.

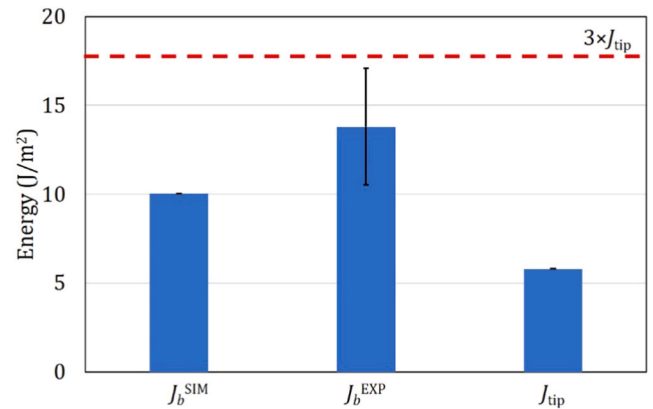


Fig. 20. Comparison of crack bridging complementary energy of RL15 and the required energy at the crack tip (standard deviation is indicated for experimental results); dashed line indicates the minimum required complementary energy for strain hardening (For interpretation of the references to colour in this figure legend, the reader is referred to the web version of this article.).

three times higher than J_{tip} to obtain a saturated multiple cracking behavior. Similarly, in this study such energy requirement is also adopted. As can be seen from Fig. 20, the complementary energy of RL15 obtained from experiment J_b^{EXP} (13.80 J/m^2) and simulation J_b^{SIM} (10.02 J/m^2) are lower than the required energy $3 \times J_{tip}$ (17.4 J/m^2 , marked by red dash line in Fig. 20). As a result, although after the first cracking a hardening branch can be found on the stress-strain curve the typical multiple cracking behavior of SHCCs multiple cracking behavior could not be obtained by RL15 both from experiments and simulation observations.

Some potential methods can be used to increase the complementary energy such as increasing the reinforcement strength and reinforcing ratio. In order to verify the multiple cracking criteria defined by the complementary energy J_b is valid, additional numerical simulations were performed. In these simulations, the strength of the reinforcement f_r was assumed to be 30 MPa, 35 MPa and 40 MPa respectively, meanwhile maintaining the elastic modulus as 1590 MPa. Then the calculated complementary J_b will be 14.43 J/m^2 , 19.63 J/m^2 and 25.65 J/m^2 , respectively. In this sense, only when f_r is not less than 35 MPa, the J_b satisfies the requirement $3 \times J_{tip}$ (17.4 J/m^2). As shown in Fig. 21, when the reinforcement material strength f_r is 25 MPa (i.e. the reinforcement material used in this study) and 30 MPa, the reinforcement breaks at the deflection $d = 1 \text{ mm}$ and eventually only one crack was obtained. Comparatively, when reinforcement material strength f_r is increased up to 35 MPa and 40 MPa, the complementary energy J_b is higher than $3 \times J_{tip}$, then the reinforcement does not completely break at $d = 1 \text{ mm}$

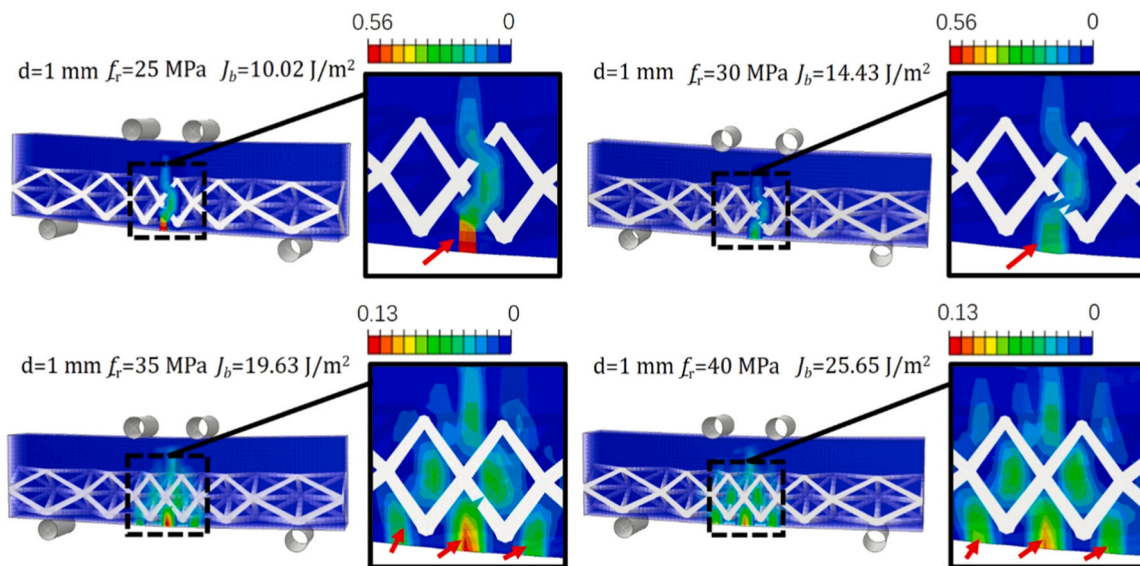


Fig. 21. Cracking of specimens reinforced by materials with different strength, cracks a indicated by red arrow (For interpretation of the references to colour in this figure legend, the reader is referred to the web version of this article.).

and multiple cracks occur (indicated by red arrow in Fig. 21). In addition, because the energy requirement is satisfied in these two cases, the crack development is closer to the so-called steady state cracking with finer crack openings.

The possibility of creating SHCCs by increasing the strength instead of the elastic modulus is rather important for 3D printed polymeric materials. On the one hand, for reinforced cementitious materials, normally very high E-modulus of the reinforcement is required to achieve multiple cracking behavior [42,43]. However, for 3D printable polymeric materials, E-modulus is physically limited because of their molecular nature. On the other hand, modifying the strength of 3D printed polymeric materials is easier. By modifying the printing parameters [39,44,45] and post processing [46,47], strength of the printed material can be obviously improved.

5. Conclusions

This work investigates the mechanical behavior of cementitious composites reinforced by 3D printed functionally grade lattice structures. Adopting functionally grading, four types of octet lattice structures are designed according to the bending moment and tensile stress distribution of flexural loaded cementitious specimens. The designed lattice structures are 3D printed using polymeric material ABS and used as reinforcement for cementitious mortar. Combining experimental, numerical and analytical studies, the flexural properties and fracture behavior of the reinforced cementitious composites are investigated. Based on the obtained results, several conclusions are drawn as follows:

- The experimental and numerical results indicate that the failure behavior of cementitious composites reinforced by 3D printed lattice structures was altered from brittle cracking to ductile failure. The ductility of the reinforced cementitious composites was significantly increased comparing to plain cementitious material in terms of ductile failure strength and total work of rupture.
- The functionally grading method proved to be very efficient in modifying flexural performance of the reinforced cementitious composites. The functionally graded reinforcement lattice structures use significantly less material while having even higher normalized ductility. In our study, an optimal case (RL15) is reducing 47.48% of reinforcement material meanwhile increasing 57.18% of normalized

ductile failure strength and 50.03% of normalized total work of rupture.

- According to the analytical results, crack bridging complementary energy J_b of the reinforced cementitious composites used in this study is lower than the required energy J_{tip} . As a result, although a hardening branch can be found in the stress-deflection curve of the cementitious composites, multiple cracking and strain hardening behavior are not achieved.
- According to the analytical model and numerical simulation results, $3 \times J_{tip}$ is the minimum required energy for the lattice structure reinforced cementitious composites to achieve multiple cracking and strain hardening behavior. Informed from the simulation results, by increasing the strength of the reinforcement material from 25 MPa to higher than 35 MPa the energy requirement could be satisfied.

This study mainly focuses on structural modification of the lattice reinforcement to improve mechanical properties of the reinforced cementitious composites. The proposed approach has shown great potential however, many aspects can be further improved. For example, as shown in the last section, multiple cracking and strain hardening can be achieved by increasing reinforcement strength without need for higher E-modulus. This is rather important for creating SHCCs with 3D printed polymeric materials because the E-modulus of 3D printable polymeric materials is rather limited by their inherent molecular nature however, their strength can be improved by, such as, modifying printing parameters and post processing. This needs to be investigated further in the future.

CRediT authorship contribution statement

Yading Xu: Investigation, Data curation, Formal analysis, Validation, Visualization, Methodology, Writing - original draft, Writing - review & editing. **Hongzhi Zhang:** Investigation, Methodology, Writing - review & editing. **Yidong Gan:** Investigation, Methodology, Writing - review & editing. **Branko Šavija:** Supervision, Investigation, Methodology, Writing - review & Editing.

Declaration of Competing Interest

The authors declare that they have no known competing financial interests or personal relationships that could have appeared to influence

the work reported in this paper.

Acknowledgements

Yading Xu and Yidong Gan would like to acknowledge the funding supported by China Scholarship Council (CSC) under the grant No. 201708110187 and No. 201706130140. The authors would like to acknowledge Mr. Jordi van Veen for his help in the sample preparing and mechanical tests.

References

- [1] Y. Xu, H. Zhang, E. Schlangen, M. Luković, B. Šavija, Cementitious cellular composites with auxetic behavior, *Cem. Concr. Compos.* 111 (2020), 103624.
- [2] G. Gibbons, 3D printing of cement composites, *Adv. Appl. Ceram.* 109 (5) (2010) 287–290.
- [3] R.A. Buswell, W.R. Leal de Silva, S.Z. Jones, J. Dirrenberger, 3D printing using concrete extrusion: a roadmap for research, *Cem. Concr. Res.* 112 (2018) 37–49.
- [4] D. Asprone, F. Auricchio, C. Menna, V. Mercuri, 3D printing of reinforced concrete elements: technology and design approach, *Constr. Build. Mater.* 165 (2018) 218–231.
- [5] J.G.Mv Mier, *Fracture Processes of Concrete*, CRC press, 1997.
- [6] J.G.Mv Mier, *Concrete Fracture: A Multiscale Approach*, CRC press, 2012.
- [7] B. Šavija, M. Luković, J. Pacheco, E. Schlangen, Cracking of the concrete cover due to reinforcement corrosion: a two-dimensional lattice model study, *Constr. Build. Mater.* 44 (2013) 626–638.
- [8] B. Šavija, M. Luković, S.A.S. Hosseini, J. Pacheco, E. Schlangen, Corrosion induced cover cracking studied by X-ray computed tomography, nanoindentation, and energy dispersive X-ray spectrometry (EDS), *Mater. Struct.* 48 (7) (2014) 2043–2062.
- [9] B. Šavija, E. Schlangen, J. Pacheco, S. Millar, T. Eichler, G. Wilsch, Chloride ingress in cracked concrete: a laser induced breakdown spectroscopy (LIBS) study, *J. Adv. Concr. Technol.* 12 (10) (2014) 425–442.
- [10] A. Blagojević, The influence of cracks on the durability and service life of reinforced concrete structures in relation to chloride-induced corrosion: a look from a different perspective, Delft University of Technology, Delft, 2016.
- [11] P.P. Win, M. Watanabe, A. Machida, Penetration profile of chloride ion in cracked reinforced concrete, *Cem. Concr. Res.* 34 (7) (2004) 1073–1079.
- [12] V.C.Li, *On engineered cementitious composites (ECC)*, 2003.
- [13] M. Luković, H. Dong, B. Šavija, E. Schlangen, G. Ye, K. Breugel, Tailoring strain-hardening cementitious composite repair systems through numerical experimentation, *Cem. Concr. Compos.* 53 (2014) 200–213.
- [14] P. Stähli, R. Custer, J.G.M. van Mier, On flow properties, fibre distribution, fibre orientation and flexural behaviour of FRC, *Mater. Struct.* 41 (1) (2007) 189–196.
- [15] P. Purnell, J. Beddows, Durability and simulated ageing of new matrix glass fibre reinforced concrete, *Cem. Concr. Compos.* 27 (9–10) (2005) 875–884.
- [16] H.R. Pakravan, M. Latifi, M. Jamshidi, Hybrid short fiber reinforcement system in concrete: a review, *Constr. Build. Mater.* 142 (2017) 280–294.
- [17] V. Mechtcherine, Novel cement-based composites for the strengthening and repair of concrete structures, *Constr. Build. Mater.* 41 (2013) 365–373.
- [18] V.C. Li, C. Wu, S. Wang, A. Ogawa, T. Saito, Interface Tailoring for Strain-Hardening Polyvinyl Alcohol-Engineered Cementitious Composite (PVA-ECC), *ACI Mater. J.* 99 (5) (2002) 463–472.
- [19] V.C. Li, F.P. Bos, K. Yu, W. McGee, T.Y. Ng, S.C. Figueiredo, K. Nefs, V. Mechtcherine, V.N. Nerella, J. Pan, G.P.A.G. van Zijl, P.J. Kruger, On the emergence of 3D printable Engineered, Strain Hardening Cementitious Composites (ECC/SHCC), *Cem. Concr. Res.* 132 (2020), 106038.
- [20] D.G. Soltan, V.C. Li, A self-reinforced cementitious composite for building-scale 3D printing, *Cem. Concr. Compos.* 90 (2018) 1–13.
- [21] S. Chaves Figueiredo, C. Romero Rodríguez, Z.Y. Ahmed, D.H. Bos, Y. Xu, T. M. Salet, O. Çopuroğlu, E. Schlangen, F.P. Bos, An approach to develop printable strain hardening cementitious composites, *Mater. Des.* 169 (2019), 107651.
- [22] J.H. Lim, B. Panda, Q.-C. Pham, Improving flexural characteristics of 3D printed geopolymer composites with in-process steel cable reinforcement, *Constr. Build. Mater.* 178 (2018) 32–41.
- [23] Z. Li, L. Wang, G. Ma, Mechanical improvement of continuous steel microcable reinforced geopolymer composites for 3D printing subjected to different loading conditions, *Compos. Part B Eng.* 187 (2020), 107796.
- [24] V. Mechtcherine, J. Grafe, V.N. Nerella, E. Spaniol, M. Hertel, U. Füssel, 3D-printed steel reinforcement for digital concrete construction – manufacture, mechanical properties and bond behaviour, *Constr. Build. Mater.* 179 (2018) 125–137.
- [25] X. Feng, F. Xue, T. Wang, L. Wang, T. Zhao, X. Liu, Reinforcing effects of 3D printed bolts on joint-separated standard soft rock specimens, *Compos. Part B Eng.* 193 (2020), 108024.
- [26] I. Farina, F. Fabbrocino, G. Carpentieri, M. Modano, A. Amendola, R. Goodall, L. Feo, F. Fraternali, On the reinforcement of cement mortars through 3D printed polymeric and metallic fibers, *Compos. Part B Eng.* 90 (2016) 76–85.
- [27] I. Farina, F. Fabbrocino, F. Colangelo, L. Feo, F. Fraternali, Surface roughness effects on the reinforcement of cement mortars through 3D printed metallic fibers, *Compos. Part B Eng.* 99 (2016) 305–311.
- [28] H.Y. Sarvestani, A.H. Akbarzadeh, H. Niknam, K. Hermenean, 3D printed architected polymeric sandwich panels: energy absorption and structural performance, *Compos. Struct.* (2018).
- [29] T.D. Ngo, A. Kashani, G. Imbalzano, K.T.Q. Nguyen, D. Hui, Additive manufacturing (3D printing): a review of materials, methods, applications and challenges, *Compos. Part B Eng.* 143 (2018) 172–196.
- [30] S. Bhandari, R. Lopez-Anido, Finite element analysis of thermoplastic polymer extrusion 3D printed material for mechanical property prediction, *Addit. Manuf.* 22 (2018) 187–196.
- [31] J. Hollander, R. Hakala, J. Suominen, N. Moritz, J. Yliruusi, N. Sandler, 3D printed UV light cured polydimethylsiloxane devices for drug delivery, *Int. J. Pharm.* 544 (2) (2018) 433–442.
- [32] B.G. Compton, J.A. Lewis, 3D-printing of lightweight cellular composites, *Adv. Mater.* 26 (34) (2014) 5930–5935.
- [33] Y. Xu, B. Šavija, Development of strain hardening cementitious composite (SHCC) reinforced with 3D printed polymeric reinforcement: mechanical properties, *Compos. Part B: Eng.* 174 (2019), 107011.
- [34] B. Salazar, I. Williams, P. Aghdasi, C. Ostertag, H. Taylor, Bending and crack characteristics of polymer lattice-reinforced mortar. *International Congress on Polymers in Concrete*, Springer, 2018.
- [35] J. Plocher, A. Panesar, Effect of density and unit cell size grading on the stiffness and energy absorption of short fibre-reinforced functionally graded lattice structures, *Addit. Manuf.* 33 (2020), 101171.
- [36] D.S.J. Al-Saedi, S.H. Masood, M. Faizan-Ur-Rab, A. Alomarah, P. Ponnusamy, Mechanical properties and energy absorption capability of functionally graded F2BCC lattice fabricated by SLM, *Mater. Des.* 144 (2018) 32–44.
- [37] L. Bai, C. Gong, X. Chen, Y. Sun, L. Xin, H. Pu, Y. Peng, J. Luo, Mechanical properties and energy absorption capabilities of functionally graded lattice structures: experiments and simulations, *Int. J. Mech. Sci.* 182 (2020), 105735.
- [38] H. Zhou, M. Zhao, Z. Ma, D.Z. Zhang, G. Fu, Sheet and network based functionally graded lattice structures manufactured by selective laser melting: design, mechanical properties, and simulation, *Int. J. Mech. Sci.* 175 (2020), 105480.
- [39] Y. Xu, H. Zhang, B. Šavija, S. Chaves Figueiredo, E. Schlangen, Deformation and fracture of 3D printed disordered lattice materials: experiments and modeling, *Mater. Des.* 162 (2019) 143–153.
- [40] V.C. Li, From micromechanics to structural engineering - the design of cementitious composites for civil engineering applications, *J. Struct. Mech. Earthq. Eng.* 10 (2) (1993) 37–48.
- [41] T. Kanda, V. Li, Multiple cracking sequence and saturation in fiber reinforced cementitious composites, *Concr. Res. Technol.* 9 (2) (1998) 19–33.
- [42] S. Cheng, J. Ji, M. Meng, Interfacial response of fibre-to-matrix in textile reinforced concrete between two cracks: Analytical solution, *Compos. Struct.* 245 (2020), 112380.
- [43] L. Nahum, A. Peled, E. Gal, The flexural performance of structural concrete beams reinforced with carbon textile fabrics, *Compos. Struct.* 239 (2020), 111917.
- [44] A.D. Valino, J.R.C. Dizon, A.H. Espera, Q. Chen, J. Messman, R.C. Advincula, Advances in 3D printing of thermoplastic polymer composites and nanocomposites, *Prog. Polym. Sci.* 98 (2019), 101162.
- [45] Y. Ming, S. Zhang, W. Han, B. Wang, Y. Duan, H. Xiao, Investigation on process parameters of 3D printed continuous carbon fiber-reinforced thermosetting epoxy composites, *Addit. Manuf.* 33 (2020), 101184.
- [46] S. Bhandari, R.A. Lopez-Anido, D.J. Gardner, Enhancing the interlayer tensile strength of 3D printed short carbon fiber reinforced PETG and PLA composites via annealing, *Addit. Manuf.* 30 (2019), 100922.
- [47] E.R. Fitzharris, I. Watt, D.W. Rosen, M.L. Shofner, Interlayer bonding improvement of material extrusion parts with polyphenylene sulfide using the Taguchi method, *Addit. Manuf.* 24 (2018) 287–297.